



Cite as
Nano-Micro Lett.
(2020) 12:165

Received: 1 May 2020
Accepted: 22 July 2020
© The Author(s) 2020

Enhanced Pseudo-Capacitive Contributions to High-Performance Sodium Storage in TiO₂/C Nanofibers via Double Effects of Sulfur Modification

Yan Zhang¹, Yuanye Huang¹, Vesna Srot¹, Peter A. van Aken¹, Joachim Maier¹, Yan Yu^{2,3} ✉

✉ Yan Yu, yanyumse@ustc.edu.cn

¹ Max Planck Institute for Solid State Research, Stuttgart 70569, Germany

² Hefei National Laboratory for Physical Sciences at the Microscale, Department of Materials Science and Engineering, Key Laboratory of Materials for Energy Conversion, Chinese Academy of Sciences (CAS), University of Science and Technology of China, Hefei 230026, Anhui, People's Republic of China

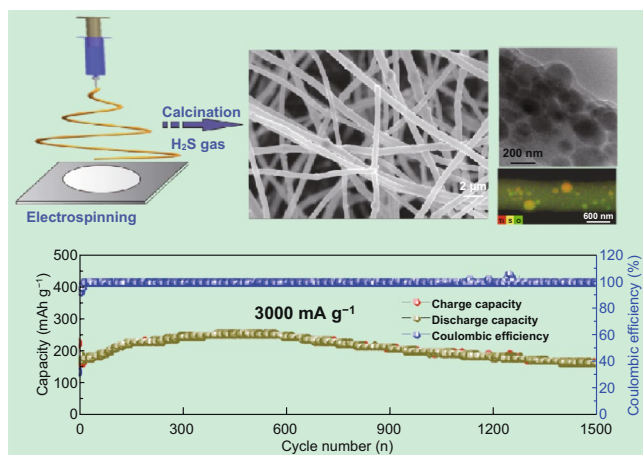
³ Dalian National Laboratory for Clean Energy (DNL), Chinese Academy of Sciences (CAS), Dalian 116023, Liaoning, People's Republic of China

HIGHLIGHTS

- One-dimensional elongated TiS₂-modified and S-doped TiO₂/C nanofibers electrode was synthesized through electrospinning, which exhibited a high specific capacity, excellent cyclic stability, and rate capability in sodium-ion battery.
- An enhanced pseudo-capacitive capacity because of S doping and TiS₂ decoration contributes to noticeable sodium storage performance. High capacity of 161 mAh g⁻¹ (at 3000 mA g⁻¹) after 1500 cycles and 58 mAh g⁻¹ (at 10,000 mA g⁻¹) after 10,000 cycles is delivered outstandingly.

ABSTRACT Pseudo-capacitive mechanisms can provide higher energy densities than electrical double-layer capacitors while being faster than bulk storage mechanisms. Usually, they suffer from low intrinsic electronic and ion conductivities of the active materials. Here, taking advantage of the combination of TiS₂ decoration, sulfur doping, and a nanometer-sized structure, as-spun TiO₂/C nanofiber composites are developed that enable rapid transport of sodium ions and electrons, and exhibit enhanced pseudo-capacitively dominated capacities. At a scan rate of 0.5 mV s⁻¹, a high pseudo-capacitive contribution (76% of the total storage) is obtained for the S-doped TiS₂/TiO₂/C electrode (termed as TiS₂/S-TiO₂/C). Such enhanced pseudo-capacitive activity allows rapid chemical kinetics and significantly improves the high-rate sodium storage performance of TiO₂. The TiS₂/S-TiO₂/C composite electrode delivers a high capacity of 114 mAh g⁻¹ at a current density of 5000 mA g⁻¹. The capacity maintains at high level (161 mAh g⁻¹) even after 1500 cycles and is still characterized by 58 mAh g⁻¹ at the extreme condition of 10,000 mA g⁻¹ after 10,000 cycles.

KEYWORDS Sodium-ion battery; Pseudo-capacitive; Anodes; TiO₂/C nanofibers; Sulfur doped



1 Introduction

Sodium-ion batteries (SIBs) are currently considered as large-scale energy storage systems potentially replacing lithium-ion batteries (LIBs) because of greater abundance and of lower cost [1, 2]. Even though the larger ion radius and higher molar mass appear to be kinetically and thermodynamically disadvantageous, the lower polarization exerted by Na^+ possesses advantages in terms of ion mobility and charge-transfer kinetics. In spite of the homologous role in the periodic system, the working chemistry of SIBs is not directly adaptable from LIBs [3, 4]. Graphitic carbon, as anode in the commercial LIBs (a capacity of 372 mAh g^{-1}), stores sodium only with a specific capacity of 31 mAh g^{-1} [5, 6]. As reported, doped graphite with enlarged layer distances (more than 0.37 nm) has been proposed as a rational solution, to more easily accommodate sodium ions between the parallel graphene sheets [7–12]. Introducing heteroatoms into the active material has also been suggested to be an effective way to promote the sodium storage performance of titanium-based materials [13–15]. For example, C-, N-doped titanium dioxide (TiO_2) can exhibit a remarkable sodium storage capacity [16]. The introduction of heteroatoms influences the thermodynamic and kinetic features by their sheer presence as well as their doping effect.

Recently, for titanium-based materials, pseudo-capacitive charge storage mechanisms have been shown to increase the overall energy storage behavior. For instance, previous work by Lukatskaya et al. showed ultrahigh-rate pseudo-capacitive energy storage in 2D $\text{Ti}_3\text{C}_2\text{T}_x$ materials (T denotes surface terminations) [17]. The TiO_2 -based insertion materials are considered as the most promising SIBs anodes [18]. Pseudo-capacitive sodium storage in a composite of nanostructured doped TiO_2 with graphene has been reported to be characterized by high-rate performance [19–21], which is enabled by improved charge transfer and electron/ion conductivities [22].

Graphene-analogous transition metal dichalcogenides (TMDC), such as MoS_2 , VS_2 , MoSe_2 , TiS_2 , NiS_2 , and CoS_2 , have been also regarded as relevant pseudo-capacitive materials with potentially improved energy storage [23]. Among these, TiS_2 is the lightest and cheapest, and owing to the lower electronegativity of sulfur, it is less ionic than TiO_2 . It has been proposed as sodium storage energy system by Winn et al. [24] and by Newman et al. [25]. It exhibits exceedingly

high electronic conductivities ($10^3 \text{ ohm}^{-1} \text{ cm}^{-1}$) [26], substantial ion diffusion rates [27], low volume expansion as well as the absence of phase change during cycling.

These assets let us develop TiS_2 -modified S-doped TiO_2/C nanofibers composites (referred as $\text{TiS}_2/\text{S-TiO}_2/\text{C}$) via electrospinning, where the carbon nanofiber acts as framework, and TiS_2 as pseudo-capacitive decoration of the TiO_2 matrix. Owing to the combination of helpful morphological and compositional features, the $\text{TiS}_2/\text{S-TiO}_2/\text{C}$ nanofibers exhibit a superb high-rate performance and long-term cycling life in SIBs.

2 Experimental Section

2.1 Materials Preparation

For electrospinning, 1.0 g polyacrylonitrile (PAN, $M_w = 150,000$, Sigma-Aldrich) was firstly dissolved in 9 mL N,N-dimethylformamide (DMF) at room temperature through vigorous stirring. Then, 1.5 mL titanium (IV) butoxide (TBOT, liquid, Sigma-Aldrich) was added to the above solution. A homogeneous precursor solution for electrospinning was prepared under strong stirring for 12 h . The resultant precursor solution was poured into a 5 mL plastic syringe connected to an 18-gauge blunt tip needle. The solution flow rate of 1 mL h^{-1} is adjusted by a syringe pump (New Era, Era-1000, USA). A voltage of 19 kV was provided by a high voltage–power supply (Model HCE35-35000, FUG DC power source, Germany). An aluminum foil was placed 15 cm below the needle as collector of the products. The as-obtained PAN-TBOT membrane was directly carbonized at $700 \text{ }^\circ\text{C}$ for 3 h with a heating rate of $5 \text{ }^\circ\text{C min}^{-1}$ in different gas atmospheres. The samples obtained in H_2S or argon gas were termed as $\text{TiS}_2/\text{S-TiO}_2/\text{C}$ or TiO_2/C .

2.2 Materials Characterization

The crystal phase of composition was measured by XRD on a Philips PW 3020 machine with $\text{Cu K}\alpha$ radiation. The structures and morphology were observed on JEOL 6300F field-emission scanning electron microscope (FESEM, Tokyo, Japan) at 15 kV . HRTEM and HAADF-STEM imaging combined with analytical EDX measurements were carried out at 200 kV with an advanced TEM (JEOL ARM200F,

JEOL Co. Ltd.), equipped with a cold field-emission gun and a CETCOR image corrector (CEOS Co. Ltd.). XPS measurements were performed with a Kratos Axis Ultra instrument using monochromatized Al $\kappa\alpha$ X-rays. (Kratos Analytical Ltd, UK). Thermogravimetric analysis was undertaken on a thermal analysis instrument (NETZSCH STA449F3, Germany). The Brunauer–Emmett–Teller (BET, BELSORP-MINI II) specific surface area was calculated according to the nitrogen adsorption–desorption curves at 77 K. The pore size distribution was determined on the basis of the Barrett–Joyner–Halenda (BJH) method.

2.3 Electrochemical Measurements

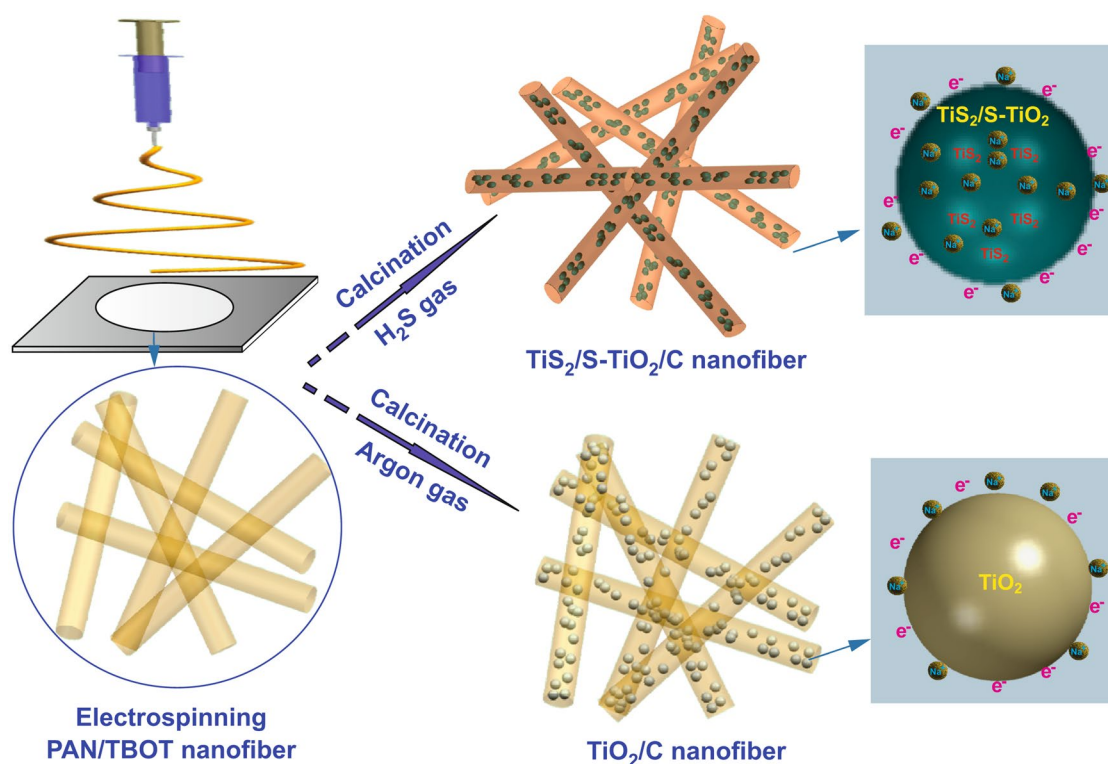
The homogenous mix slurry was made of active materials ($\text{TiS}_2/\text{S-TiO}_2/\text{C}$ or TiO_2/C), Super-P (carbon black, Timcal), and carboxymethyl cellulose (CMC, Sigma-Aldrich) binder with a weight ratio of 70:15:15. The as-prepared slurry was pasted on a copper current collector and dried in a vacuum oven for 12 h at 60 °C. In CR2032-type coin cell, the coated copper disks were used as working electrode, sodium metal

foil was used as counter/reference electrode, 1 M solution of NaClO_4 (Sigma-Aldrich, 99%) in a 95:5 vol/vol mixture of propylene carbonate (PC, Sigma-Aldrich, anhydrous 99.7%) and fluoroethylene carbonate (FEC, Sigma-Aldrich, 99%) was used as electrolyte, and a glass fiber (GF/D) was used as separator. The assembling of sodium-ion battery was finished in a MBraun glove box filled with highly pure argon gas (O_2 and H_2O levels < 0.5 ppm). The half-cell was galvanostatically discharged and charged in BTS battery test instrument (Neware BTS 7.0, Shenzhen). Cyclic voltammetry (CV) measurements were performed on Autolab instruments at various scan rates. These measurements were performed in the fixed voltage window between 3.0 and 0.01 V.

3 Results and Discussion

3.1 Crystallographic and Morphological Structure

As shown in Scheme 1, $\text{TiS}_2/\text{S-TiO}_2/\text{C}$ nanofibers were prepared by electrospinning followed by annealing of PAN-tetrabutyl orthotitanate nanofibers (termed as PAN-TBOT)



Scheme 1 Schematic illustrations of the synthesis process for $\text{TiS}_2/\text{S-TiO}_2/\text{C}$ nanofiber and TiO_2/C nanofibers

precursors in an H_2S atmosphere. TiO_2/C nanofibers without sulfur components were obtained through sintering of same precursors fibers under argon gas. For $\text{TiS}_2/\text{S-TiO}_2/\text{C}$ nanofibers, 1D nanofiber structure can provide a fast electron pathway and alleviate the volume stress; the synergistic effects of the sulfur doping and TiS_2 decoration enable fast ion/electron transfer in the TiO_2 phase and improve the interfacial storage. The XRD patterns (Figs. 1a and S1) show two samples with a typical crystalline structure of the anatase phase (PDF#21-1272); three obvious peaks at 16.0° , 34.8° ,

and 44.6° are only observed in the $\text{TiS}_2/\text{S-TiO}_2/\text{C}$ sample, corresponding to the (001), (011), and (102) crystal planes of TiS_2 , respectively (PDF#88-1967) [28, 29]. In Figs. 1 and S1, the broad and small peaks at about 26° correspond to the carbon content (marked by arrows). X-ray photoelectron spectroscopy (XPS) was performed to verify the chemical state of $\text{TiS}_2/\text{S-TiO}_2/\text{C}$ nanofibers (Fig. 1b–f). The integral survey spectrum of $\text{TiS}_2/\text{S-TiO}_2/\text{C}$ nanofibers shows O, Ti, C, N, and S components. Regarding the Ti 2p peaks, the two peaks at 458.5 and 464.2 eV are assigned to Ti $2p_{3/2}$

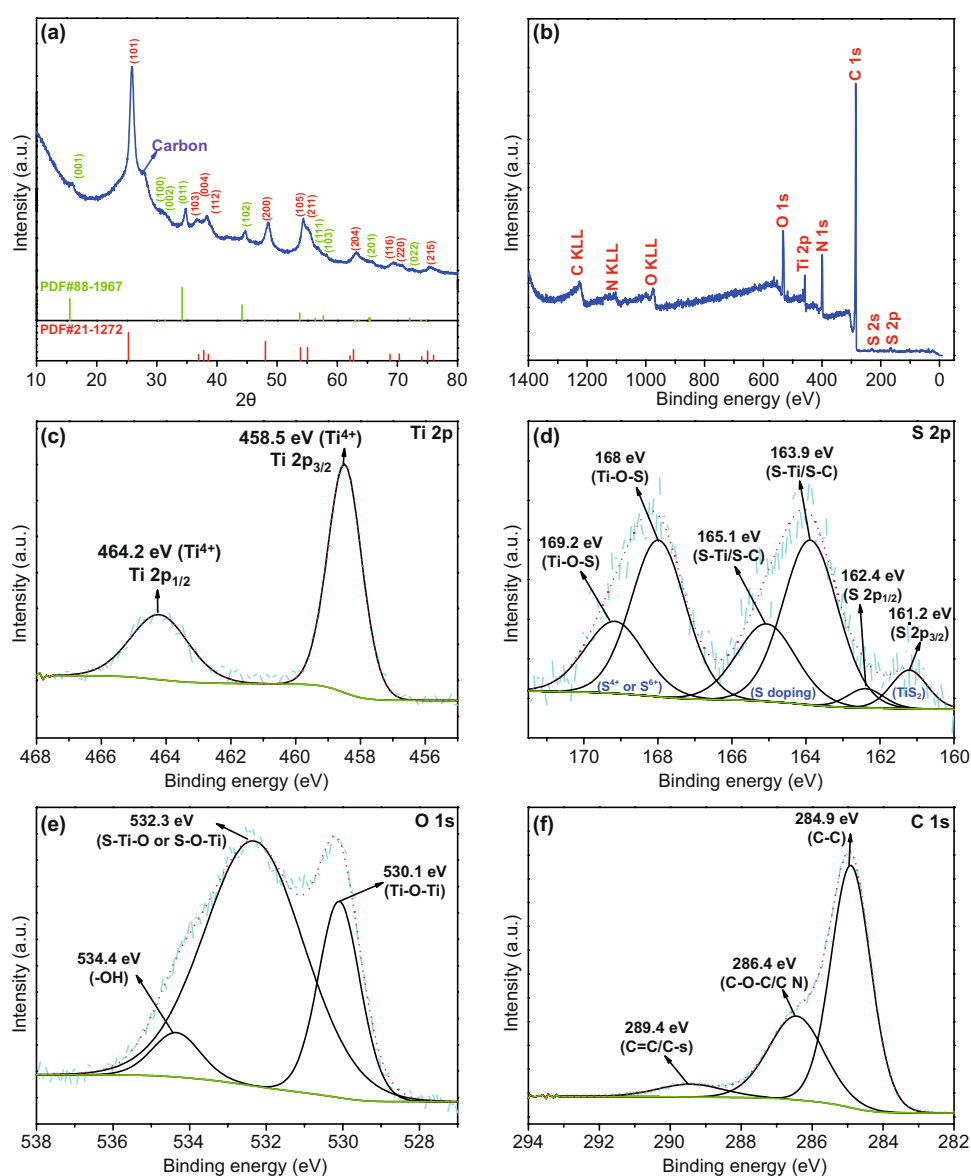


Fig. 1 a XRD patterns. b Integrated XPS spectrum. c–f High-resolution XPS spectra of Ti 2p, S 2p, O 1s, and C 1s of the as spun of $\text{TiS}_2/\text{S-TiO}_2/\text{C}$ nanofibers composites

and Ti $2p_{1/2}$ of the tetravalent Ti ion (Fig. 1c). In the high-resolution spectrum of S 2p (Fig. 1d), the chemical state of sulfur was characterized by several peaks. The low-energy ones at 161.2 and 162.4 eV can be attributed to the TiS_2 phase [30, 31]. The high-energy doublet centered at 163.9 and 165.1 eV can be correlated with S-Ti and S-C, which confirm S doping of TiO_2 bulk and of carbon fibers [32]. It is possible that the calcination in H_2S flow results in partial substitution of O by S atoms. The sulfur peaks of strong intensity at 167–170 eV suggest that sulfur replaces Ti^{4+} in the form of S^{4+} or S^{6+} [32, 33]. In line with a previous report by Devi et al., the replacement of Ti by sulfur leads to the formation of Ti–O–S bonds and is more favorable than the substitution of O^{2-} by S^{2-} [34]. The O 1s signal at 534.4 eV also confirms the presence of Ti–O–S bond (Fig. 1e). The C 1s features are assignable to C–C (284.9 eV), C=O or C=N (286.4 eV), and C–O–C or C–S bonds (289.4 eV) (Fig. 1f), which stem from the polyacrylonitrile (PAN) polymer precursor. These XPS results demonstrate the existence of TiS_2 and S defects within the TiO_2 lattice, which is expected to improve the sodium storage performance of $\text{TiS}_2/\text{S-TiO}_2/\text{C}$ composites.

The morphology and structure of as-obtained $\text{TiS}_2/\text{S-TiO}_2/\text{C}$ nanofibers are shown in Fig. 2a, b, displaying a well-dispersed and interwoven fibrous network, which is similar with the structure of PAN-TBOT precursors (Fig. S2a, b) and TiO_2/C nanofibers (Fig. S2c, d). At a larger magnification, 1D nanofibers display a uniform diameter distribution of about 600 nm, whereby some nanoparticles are aggregated inside the fibers (Fig. 2c). The bright-field (BF) transmission electron microscope (TEM) images (Fig. 2d, e) visualize these particles with sizes of several ten nanometers. In the high-resolution TEM (HRTEM) (Fig. 2f, g), the measured lattice fringe spacing of 0.36 nm corresponds to the (101) lattice plane spacing of anatase TiO_2 . The amorphous regions around the lattice fringes are ascribed to the carbon phase. The carbon nanofiber may help to improve the mechanical stability for long-term cycle operation and can serve as lead for electron transfer throughout the overall electrode. High-angle annular dark-field (HAADF) scanning TEM (STEM) image of a representative $\text{TiS}_2/\text{S-TiO}_2/\text{C}$ single nanofiber (Fig. 2i) and corresponding Ti, O, S, C (Fig. 2j–m) and overlapped Ti/S EDX elemental maps (Fig. 2n) are presented. The Ti and O EDX maps clearly exhibit enriched regions at the position of particles inside the fibers. Although sulfur is quite

homogeneously distributed within the nanofibers, S mapping exhibits a slightly enhanced concentration in the regions around the particles. Additionally, the higher signals of S, Ti, and O in the particles from the elemental maps (Fig. 2j–l) together with the XRD and XPS results confirm the presence of TiS_2 and sulfur-doped TiO_2 . The nitrogen adsorption–desorption isotherm was measured to determine the Brunauer–Emmett–Teller (BET) surface area and pore size distribution, as shown in Fig. S3a, b. It showed that the specific surface area and the average pore size of $\text{TiS}_2/\text{S-TiO}_2/\text{C}$ nanofibers were $146.1 \text{ m}^2 \text{ g}^{-1}$ and 12–17 nm, respectively, which is ascribed to the interwoven fibrous network affording a large surface area and porous structure.

3.2 Electrochemical Properties

To explore the influence of sulfur doping and TiS_2 modification on the sodium storage performance of TiO_2/C electrode, the electrochemical performance of as-spun $\text{TiS}_2/\text{S-TiO}_2/\text{C}$ nanofibers composites, TiO_2/C nanofibers composites, and pure C nanofibers as anodes in SIBs was investigated. All of the electrochemical measurements were performed at voltages of 0.01–3.0 V. Figure 3a displays the discharge–charge profile in the first five cycles for the $\text{TiS}_2/\text{S-TiO}_2/\text{C}$ electrode at a current density of 100 mA g^{-1} . In the first discharge–charge process, the $\text{TiS}_2/\text{S-TiO}_2/\text{C}$ electrode delivers an initial discharge-specific capacity of 419.6 mAh g^{-1} and charge-specific capacity of 197.2 mAh g^{-1} , which are higher than those of the TiO_2/C electrode (Fig. S4a, discharge-specific capacity: 330.7 mAh g^{-1} , charge-specific capacity: 159.8 mAh g^{-1}). Both electrodes show irreversible capacities in the first cycle, which is ascribed to the formation of a solid electrolyte interface (SEI) layer on the electrode surface and the decomposition of the electrolyte [35]. When the voltage is below 1.5 V, the two electrodes show similar voltage slopes and working voltages profile, strongly suggesting that the sodium storage contribution mainly stemmed from the TiO_2 component. Notably, a characteristic charge plateau located at higher working voltages in the range of 1.5–2.5 V is attributed to sodium extraction out of TiS_2 materials [36]. After 400 cycles, the reversible capacity of $\text{TiS}_2/\text{S-TiO}_2/\text{C}$ composites electrode maintained at 274 mAh g^{-1} (Fig. 3b), which is markedly superior to 199 mAh g^{-1} of TiO_2/C composites electrode (Fig. S4b, 400th cycle) and about 162 mAh g^{-1} of pure C nanofiber electrode (Fig. S5, 50th

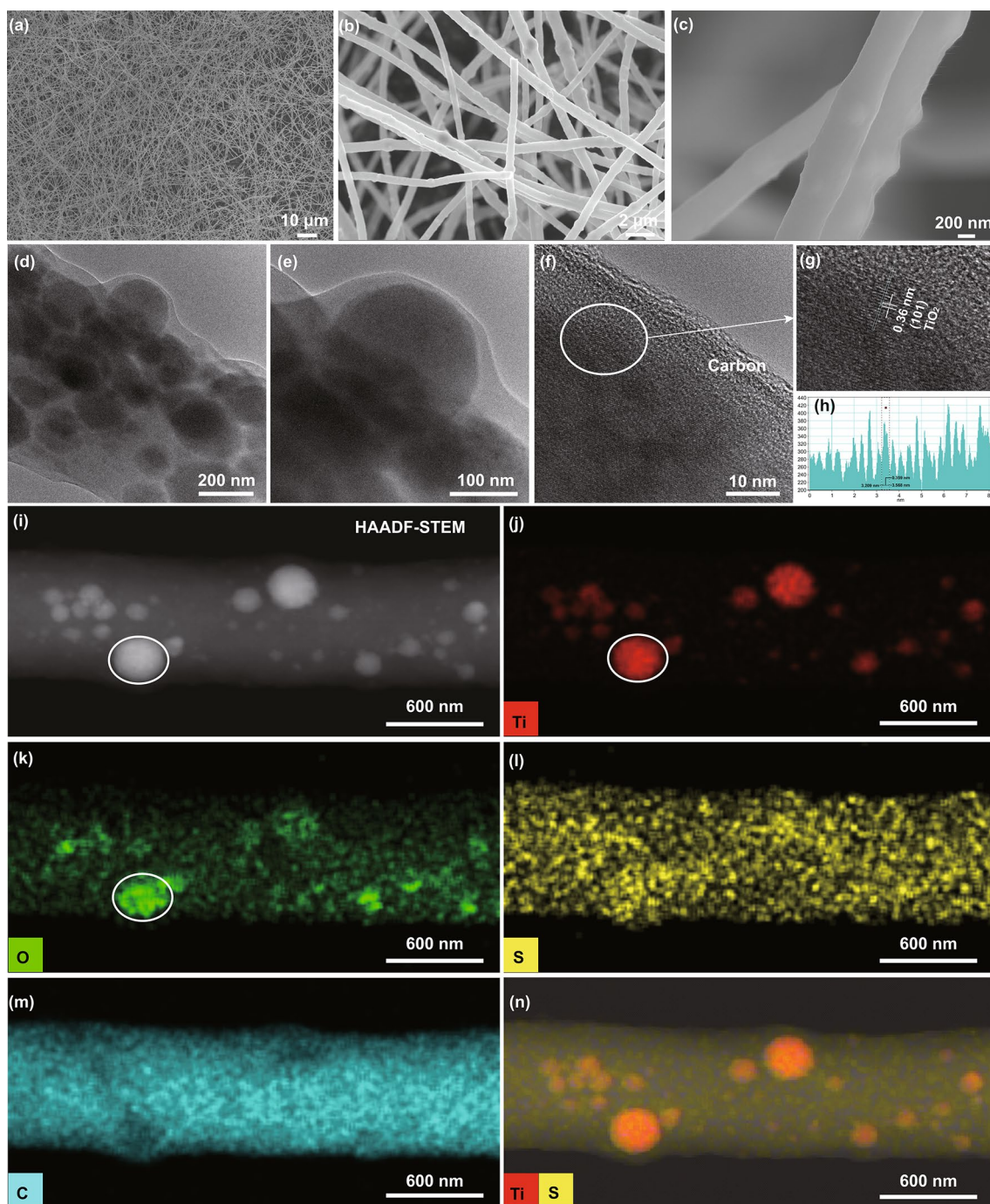


Fig. 2 a–c SEM images. d–e BF-TEM images. f–h Representative HRTEM image with indicated measured distances between the lattice planes in crystalline TiO_2 core. i HAADF-STEM image with of as-spun $\text{TiS}_2/\text{S-TiO}_2/\text{C}$ single nanofiber with the corresponding j Ti, k O, l S, m C, and n overlay of Ti and S EDX maps

cycle). After three cycles, the high Coulombic efficiency is close to 100%, demonstrating the cycling reversibility of $\text{TiS}_2/\text{S-TiO}_2/\text{C}$ electrode. Notably, good cyclability for $\text{TiS}_2/\text{S-TiO}_2/\text{C}$ composites electrode and TiO_2/C composites

electrode is closely connected with the unique structure of interwoven fibrous network with assembling nanoparticles in a nanofiber, which can be proved the morphologies after discharged and charged cycling (Fig. S8).

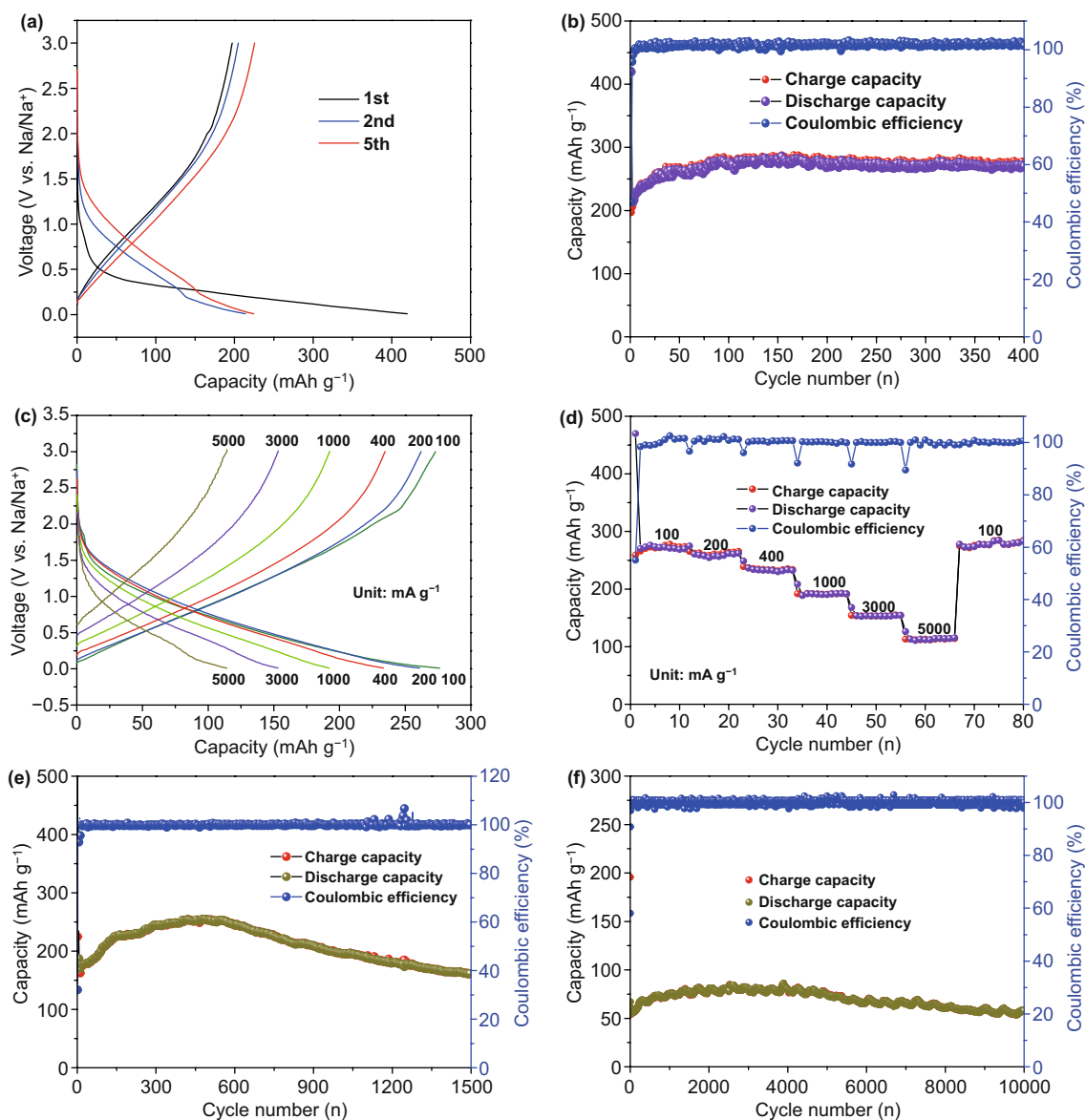


Fig. 3 **a** Charge–discharge profiles of the first, second, and fifth cycle. **b** Cycling performances at a current density of 100 mA g^{-1} . **c** Charge–discharge profiles at different rates. **d** Rate performances. **e** Cycling performance at a rate of 100 mA g^{-1} for four cycles and a rate of 3000 mA g^{-1} for 1500 times. **f** Long-term cycling performance at a rate of 100 mA g^{-1} for four cycles and a rate of $10,000 \text{ mA g}^{-1}$ for 10,000 times of $\text{TiS}_2/\text{S-TiO}_2/\text{C}$ nanofibers electrode in SIBs

As plotted in Fig. 3c, d, the rate performances of the electrodes are further evaluated at different current densities from 100 to 5000 mA g^{-1} . When increasing the current density, the $\text{TiS}_2/\text{S-TiO}_2/\text{C}$ electrode exhibits 271.4 mAh g^{-1} (100 mA g^{-1}), 258.7 mAh g^{-1} (200 mA g^{-1}), 235.5 mAh g^{-1} (400 mA g^{-1}), 191.6 mAh g^{-1} (1000 mA g^{-1}), 153.8 mAh g^{-1} (3000 mA g^{-1}), and 114.2 mAh g^{-1} (5000 mA g^{-1}), respectively, whereas the TiO_2/C electrode shows only 210.1, 175.4, 145.3, 111.9, 70.16, and 40.7 mAh g^{-1} at

the corresponding rates in Fig. S4c. When the current density is set back to 100 mA g^{-1} , the specific capacity of the $\text{TiS}_2/\text{S-TiO}_2/\text{C}$ electrode can recover to 284.9 mAh g^{-1} , indicating an outstanding rate capability. The rate performance of the $\text{TiS}_2/\text{S-TiO}_2/\text{C}$ electrode is superior to that of the TiO_2/C electrode in the entire rate range, showing the improvement of the electrochemical activity of TiO_2 with the help of the introduction of TiS_2 and S doping. When the $\text{TiS}_2/\text{S-TiO}_2/\text{C}$ electrode is cycled in 3000 mA g^{-1} for

1500 cycles, it still exhibits a high capacity of 161 mAh g⁻¹ (Fig. 3e). Most impressively, a stable capacity of 58 mAh g⁻¹ at ultrahigh current density of 10,000 mA g⁻¹ (Fig. 3f) is maintained after 10,000 cycles, indicating excellent ultralong cycling stability. To the best of our knowledge, the TiS₂/S-TiO₂/C nanofiber electrode is comparable to the best performances reported as-spun TiO₂ nanofiber anode in the literature in terms of both cycling stability and rate capability (Table 1). The improvements of the electrochemistry performance may be attributed to promoted interfacial charge-transfer kinetics of high conductivity TiS₂ and increased sodium storage sites at the TiS₂/TiO₂ grain boundaries. Moreover, the carbon nanofibers may help the mechanical stability and the electron/ion diffusivity, which synergistically improve electrochemical activity of TiO₂ at high rate.

To get a deeper insight into the electrochemical behavior of the TiS₂/S-TiO₂/C electrode, representative cyclic voltammetry (CV) measurements were carried out at a scan rate of 0.1 mV s⁻¹ in the range of 0.01–3.0 V (vs Na/Na⁺). As illustrated in Fig. 4a, for two electrodes, the peak at 1.0–1.2 V is only observed in the first cathodic scan, which is ascribable to a typically irreversible reaction associated with the decomposition of the electrolyte and the formation of a solid electrolyte interface (SEI). A couple of broad redox peaks that appeared below 1.5 V suggest that the reversible reaction of Ti³⁺/Ti⁴⁺ takes place during sodium insertion/extraction into/out of the crystal structure of TiO₂ [37–39]. At high voltages of 1.5–3.0 V, the TiS₂/S-TiO₂/C electrode shows one reductive peak (1.60 V) and two oxidative peaks (–1.6 and 2.2 V) in the following four scans

(Figs. 4a and S6a), corresponding to multiple reversible phase transitions during sodiation/desodiation of TiS₂. This observation is in good agreement with the behavior of the reported pure TiS₂ electrode, being indicative of the formation of Na_{0.22}TiS₂, Na_{0.55}TiS₂, or NaTiS₂ phase [36]. It is notable that when TiS₂ and S are incorporated, the composite electrodes show a small increase in the area of CV curves above 1.5 V, but a significant increase in the area of closed curves below 1.5 V. The results indicate not only that the enhancement of sodium storage of TiS₂/S-TiO₂/C nanofibers may originate from the storage contribution of incorporated TiS₂, but also show the significance for the synergistic improvement of the electrochemical activity of TiO₂. In order to gain further insight into the synergistic influences of TiS₂ modification and S doping, a kinetic analysis on the basis of CV at various scan rates ranging from 0.1 to 100 mV s⁻¹ is evaluated (Figs. S6b–c and S7a–c). In general, the reaction kinetics mechanism is divided into the two typical types of (i) diffusion-controlled process and (ii) capacitive-controlled behavior, whereby the former refers to the faradaic redox reaction from sodium-ion intercalation and the latter indicates surface faradaic pseudo-capacitive as well as non-faradaic double-layer contributions. The charge storage mechanism inferred from the parameter *b* is the relation ($i = av^b$) (*a* and *b* are adjustable parameters) between peak current response (*i*) and the scan rates (*v*) [40]. When *b*, i.e., the slope of log(*i*) – log(*v*) plot, is close to 0.5 (*b* = 0.5), diffusion-controlled faradaic intercalation is suggested. The value being close to 1 (*b* = 1) signifies pseudo-capacitive storage kinetics. Figure 4b displays the log(*i*) – log(*v*) plots

Table 1 Comparison of the sodium storage performances of as-spun TiS₂/S-TiO₂/C nanofibers with previously reported electrospun TiO₂ nanofiber anode in SIBs

Materials	High-rate capacity (mAh g ⁻¹)	Cycle performances (mAh g ⁻¹)	Initial Coulombic efficiency	Publication years
TiO ₂ /C nanofibers [46]	164.9 at 2000 mA g ⁻¹	237.1 at 200 mA g ⁻¹ over 1000 cycles;	58%	2016
N-doped anatase TiO ₂ nanofibers [47]	110 at 3350 mA g ⁻¹	110 at 3350 mA g ⁻¹ over 500 cycles;	/	2016
TiO _{2-x} nanocages anchored carbon fiber [48]	120 at 1000 mA g ⁻¹	150 at 1000 mA g ⁻¹ over 1000 cycles;	38.3%	2018
Amorphous black TiO _{2-x} /C nanofiber [49]	61 at 415 mA g ⁻¹	90 at 16.6 mA g ⁻¹ over 100 cycles;	/	2018
TiS ₂ /S-TiO ₂ /C nanofibers (this work)	114.2 at 5000 mA g ⁻¹	161 at 3000 mA g ⁻¹ over 1500 cycles; 58 at 10,000 mA g ⁻¹ over 10,000 cycles	47%	/

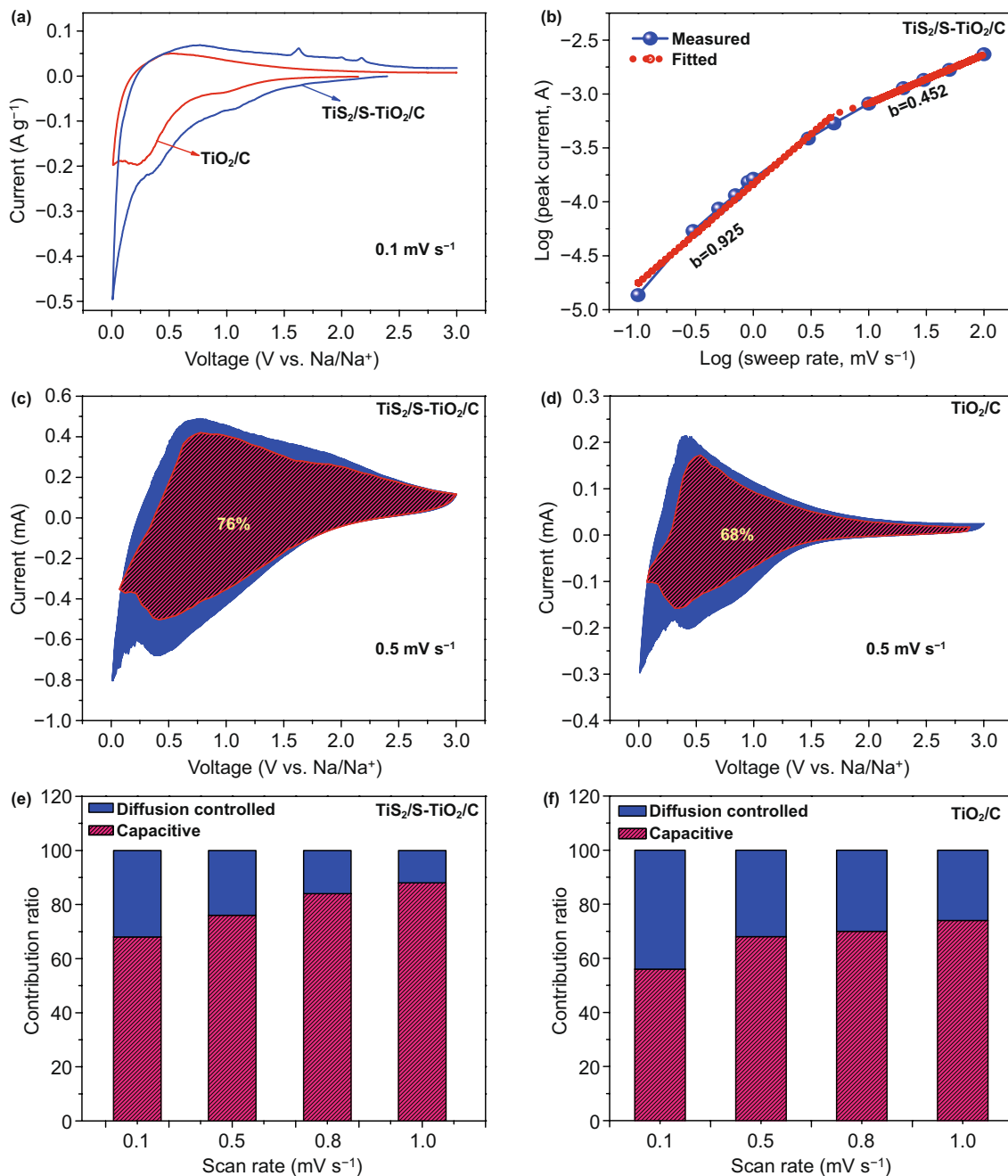


Fig. 4 **a** CV curve of the first cycle at 0.1 mV s^{-1} . **b** Relationship between $\log(i)$ and $\log(v)$. **c, d** Pseudo-capacitive contribution at 0.5 mV s^{-1} . **e, f** The ratio of pseudo-capacitive contribution (pink) at various scan rates of electrochemical impedance spectroscopy plots of $\text{TiS}_2/\text{S-TiO}_2/\text{C}$ nanofibers electrode and TiO_2/C nanofibers electrode in SIBs

of the $\text{TiS}_2/\text{S-TiO}_2/\text{C}$ electrode, where obviously b changes from 0.925 (at scan rates of 0.1 to 1 mV s^{-1}) to 0.452 (at scan rates of 3 to 100 mV s^{-1}). Obviously, the sodium storage mechanism of $\text{TiS}_2/\text{S-TiO}_2/\text{C}$ is dominated by surface pseudo-capacitive behavior at low rates and then turns to a

diffusion-controlled process at fast scans, which is in coincidence with the pseudo-capacitive storage phenomenon of $\text{T-Nb}_2\text{O}_5/\text{Li}$ cell by Dunn et al. [41].

Furthermore, the ratios of the pseudo-capacitive storage capacity contribution in the total charge storage are

calculated from $i(V) = k_1 v + k_2 v^{1/2}$ [42]. Here, the quantitative indicators of the pseudo-capacitive and diffusive contributions are k_1 and k_2 , which can be obtained on the basis of the current response at a particular voltage. As can be seen in Fig. 4c, at a scan rate of 0.5 mV s^{-1} the ratio of the pseudo-capacitive contribution for the $\text{TiS}_2/\text{S-TiO}_2/\text{C}$ electrode is as high as 76%, which is higher than that of the TiO_2/C electrode (Fig. 4d). Additionally, as indicated by the shadowed area shown in Figs. 4e and S6d-f, at low scan rates ranging from 0.1 to 1 mV s^{-1} , the pseudo-capacitive contribution gradually increases from 68 to 88% with increasing scan rates. Similarly, at a given scan rate, the pseudocapacitance rates of the TiO_2/C electrode are also calculated, exhibiting a lower surface pseudo-capacitive contribution (Figs. 4f and S7d-f). Such observation demonstrates the enhancement of the pseudo-capacitive contribution as a result of the introduction of TiS_2 and S doping, similar to the reported pseudo-capacitive MoO_2 -modified TiO_2 composites [43] and doped TiO_2 materials [20, 44]. Here, the combination of pseudo-capacitive TiS_2 and sulfur doping can further increase the pseudo-capacitive contribution to the total capacity.

To further deeply the influence of sulfur doping and TiS_2 modification, the sodium-ion diffusion coefficient has been investigated according to a cyclic voltammetry (CV) method, with the basis of the following equation: $I_p = \Delta 0.4463zFA(zF/RT)^{1/2} \Delta C_0 D_{\text{Na}}^{1/2} v^{1/2}$ [45]. Here, R is the gas constant, T is the absolute temperature, ΔC_0 is the surface concentration of the electrode material, while I_p and v represent peak current and scan rate, respectively. The sodium-ion diffusion coefficient can be determined by the peak current (I_p) versus $v^{1/2}$ based on the Randles–Sevcik equation. The apparent sodium diffusion coefficients of the $\text{TiS}_2/\text{S-TiO}_2/\text{C}$ electrode are calculated to be $8.34 \times 10^{-10} \text{ cm}^2 \text{ s}^{-1}$, which is higher than D_{Na} values of TiO_2/C electrode ($5.82 \times 10^{-10} \text{ cm}^2 \text{ s}^{-1}$) without any sulfur content (Fig. S9). It suggests that the D_{Na} of the $\text{TiS}_2/\text{S-TiO}_2/\text{C}$ electrode can be further improved by the synergistic effect of sulfur dopant and TiS_2 modification.

Such pronounced pseudo-capacitive sodium storage mechanism could be related to the combination of nanostructured and pseudo-capacitive components of $\text{TiS}_2/\text{S-TiO}_2/\text{C}$ composites electrode. The nanometer-sized $\text{TiS}_2/\text{TiO}_2$ composites can greatly improve the ion diffusivity and enhance the density at interfacial storage sites in the surface/near surface. The measured pseudo-capacitive storage behavior

allows to a fast uptake/release of the sodium ion and long cycle life at ultrahigh rate for $\text{TiS}_2/\text{S-TiO}_2/\text{C}$ electrodes.

4 Conclusions

In summary, we developed a $\text{TiS}_2/\text{S-TiO}_2/\text{C}$ composite as a superior potential electrode for SIBs with astonishing high-rate capacities and long-term cycling stabilities. The $\text{TiS}_2/\text{S-TiO}_2$ nanoparticles embedded in carbon nanofibers are obtained through electrospinning followed by a calcination in H_2S gas. The decoration of TiO_2 by TiS_2 and by sulfur doping, together with the integration into a carbon nanofibers framework, greatly improves the pseudo-capacitive behavior. As a result, the as-spun $\text{TiS}_2/\text{S-TiO}_2/\text{C}$ electrode exhibits a reversible capacity of 274 mAh g^{-1} at 100 mA g^{-1} for over 400 cycles. Even at a high rate of $10,000 \text{ mA g}^{-1}$ after 10,000 cycles, it still maintains a capacity of 58 mA g^{-1} without noticeable fading.

Acknowledgements This work was financially supported by National Key R&D Program of China (No. 2018YFB0905400), the National Natural Science Foundation of China (Nos. 51925207, 51872277, and U1910210), Dalian National Laboratory For Clean Energy (DNL) Cooperation Fund, the CAS (DNL180310), and the Fundamental Research Funds for the Central Universities (Wk2060140026) and the Sofja Kovalevskaja award of the Humboldt Society. This project has received funding from the European Union's Horizon 2020 research and innovation programme under Grant Agreement No. 823717-ESTEEM3. The authors appreciate support by Dr. Hanns-Ulrich Habermeier (carefully reading), Dr. Helga Hoier (XRD measurement), and Annette Fuchs (SEM measurement). Support by the Surface Science Central Facility (Dr. K.Müller and Dr. U. Stark) is gratefully acknowledged.

Open Access This article is licensed under a Creative Commons Attribution 4.0 International License, which permits use, sharing, adaptation, distribution and reproduction in any medium or format, as long as you give appropriate credit to the original author(s) and the source, provide a link to the Creative Commons licence, and indicate if changes were made. The images or other third party material in this article are included in the article's Creative Commons licence, unless indicated otherwise in a credit line to the material. If material is not included in the article's Creative Commons licence and your intended use is not permitted by statutory regulation or exceeds the permitted use, you will need to obtain permission directly from the copyright holder. To view a copy of this licence, visit <http://creativecommons.org/licenses/by/4.0/>.

Electronic supplementary material The online version of this article (<https://doi.org/10.1007/s40820-020-00506-1>) contains supplementary material, which is available to authorized users.

References

- B. Dunn, H. Kamath, J. Tarascon, Electrical energy storage for the grid: a battery of choices. *Science* **334**(6058), 928–935 (2011). <https://doi.org/10.1126/science.1212741>
- M.S. Islam, C.A.J. Fisher, Lithium and sodium battery cathode materials: computational insights into voltage, diffusion and nanostructural properties. *Chem. Soc. Rev.* **43**(1), 185–204 (2014). <https://doi.org/10.1039/C3CS60199D>
- J. Deng, W. Luo, S. Chou, H. Liu, S. Dou, Sodium-ion batteries: from academic research to practical commercialization. *Adv. Energy Mater.* **8**(4), 1701428 (2017). <https://doi.org/10.1002/aenm.201701428>
- W. Luo, F. Shen, C. Bommier, H. Zhu, X. Ji, L. Hu, Na-ion battery anodes: materials and electrochemistry. *Acc. Chem. Res.* **49**(2), 231–240 (2016). <https://doi.org/10.1021/acs.accounts.5b00482>
- M. Doeff, Y. Ma, S. Visco, L. De Jonghe, Electrochemical insertion of sodium into carbon. *J. Electrochem. Soc.* **140**(12), L169–L170 (1993). <https://doi.org/10.1149/1.2221153>
- H. Tao, L. Xiong, S. Du, Y. Zhang, X. Yang, L. Zhang, Interwoven N and P dual-doped hollow carbon fibers/graphitic carbon nitride: an ultrahigh capacity and rate anode for Li and Na ion batteries. *Carbon* **122**, 54–63 (2017). <https://doi.org/10.1016/j.carbon.2017.06.040>
- W. Luo, Y. Wang, L. Wang, W. Jiang, S. Chou et al., Silicon/mesoporous carbon/crystalline TiO₂ nanoparticles for highly stable lithium storage. *ACS Nano* **10**(11), 10524–10532 (2016). <https://doi.org/10.1002/acs.nano.6b06517>
- Y. Cao, L. Xiao, M. Sushko, W. Wang, B. Schwenzer et al., Sodium ion insertion in hollow carbon nanowires for battery applications. *Nano Lett.* **12**(7), 3783–3787 (2012). <https://doi.org/10.1021/nl3016957>
- H. Hou, L. Shao, Y. Zhang, G. Zou, J. Chen, X. Ji, Large-area carbon nanosheets doped with phosphorus: a high-performance anode material for sodium-ion batteries. *Adv. Sci.* **4**(1), 1600243 (2016). <https://doi.org/10.1002/advs.201600243>
- W. Hong, Y. Zhang, L. Yang, Y. Tian, P. Ge et al., Carbon quantum dot micelles tailored hollow carbon anode for fast potassium and sodium storage. *Nano Energy* **65**, 104038 (2019). <https://doi.org/10.1016/j.nanoen.2019.104038>
- H. Hou, C. Banks, M. Jing, Y. Zhang, X. Ji, Carbon quantum dots and their derivative 3D porous carbon frameworks for sodium-ion batteries with ultralong cycle life. *Adv. Mater.* **27**(47), 7861–7866 (2015). <https://doi.org/10.1002/adma.201503816>
- T. Wu, C. Zhang, G. Zou, J. Hu, L. Zhu et al., The bond evolution mechanism of covalent sulfurized carbon during electrochemical sodium storage process. *Sci. China Mater.* **62**(8), 1127–1138 (2019). <https://doi.org/10.1007/s40843-019-9418-8>
- W. Wang, Y. Liu, X. Wu, J. Wang, L. Fu et al., Advances of TiO₂ as negative electrode materials for sodium-ion batteries. *Adv. Mater. Technol.* **3**(9), 1800004 (2018). <https://doi.org/10.1002/admt.201800004>
- Y. Zhang, Z. Ding, W. Christopher, C. Banks, X. Qiu, X. Ji, Oxygen vacancies evoked blue TiO₂(B) nanobelts with efficiency enhancement in sodium storage behaviors. *Adv. Funct. Mater.* **27**(27), 1700856 (2017). <https://doi.org/10.1002/adfm.201700856>
- B. Wang, F. Zhao, G. Du, S. Porter, Y. Liu et al., Boron-doped anatase TiO₂ as a high-performance anode material for sodium-ion batteries. *ACS Appl. Mater. Interfaces* **8**(25), 16009–16015 (2016). <https://doi.org/10.1021/acsami.6b03270>
- Y. Zhang, C. Wang, H. Hou, G. Zou, X. Ji, Nitrogen doped/carbon tuning yolk-like TiO₂ and its remarkable impact on sodium storage performances. *Adv. Energy Mater.* **7**(4), 1600173 (2016). <https://doi.org/10.1002/aenm.201600173>
- M. Lukatskaya, S. Kota, Z. Lin, M. Zhao, N. Shpigel et al., Ultra-high-rate pseudocapacitive energy storage in two-dimensional transition metal carbides. *Nat. Energy* **2**, 17105 (2017). <https://doi.org/10.1038/nenergy.2017.105>
- H. Xiong, M. Slater, M. Balasubramanian, C. Johnson, T. Rajh, Amorphous TiO₂ nanotube anode for rechargeable sodium ion batteries. *J. Phys. Chem. Lett.* **2**(20), 2560–2565 (2011). <https://doi.org/10.1021/jz2012066>
- C. Chen, Y. Wen, X. Hu, X. Ji, M. Yan et al., Na⁺ intercalation pseudocapacitance in graphene-coupled titanium oxide enabling ultra-fast sodium storage and long-term cycling. *Nat. Commun.* **6**, 6929 (2015). <https://doi.org/10.1038/ncomms7929>
- H. Zhang, Y. Jiang, Z. Qi, X. Zhong, Y. Yu, Sulfur doped ultrathin anatase TiO₂ nanosheets/graphene nanocomposite for high-performance pseudocapacitive sodium storage. *Energy Storage Mater.* **12**, 37–43 (2018). <https://doi.org/10.1016/j.ensm.2017.11.008>
- Z. Le, F. Liu, P. Nie, X. Li, X. Liu et al., Pseudocapacitive sodium storage in mesoporous single-crystal-like TiO₂-graphene nanocomposite enables high-performance sodium-ion capacitors. *ACS Nano* **11**(3), 2952–2960 (2017). <https://doi.org/10.1021/acs.nano.6b08332>
- J. Kang, S. Zhang, Z. Zhang, Three-dimensional binder-free nanoarchitectures for advanced pseudocapacitors. *Adv. Mater.* **29**(48), 1700515 (2017). <https://doi.org/10.1002/adma.201700515>
- Y. Zhang, H. Tao, S. Du, X. Yang, Conversion of MoS₂ to a ternary MoS_{2-x}Se_x alloy for high-performance sodium-ion batteries. *ACS Appl. Mater. Interfaces* **11**(12), 11327–11337 (2019). <https://doi.org/10.1021/acsami.8b19701>
- D. Winn, J. Shemilt, B. Steele, Titanium disulphide: a solid solution electrode for sodium and lithium. *Mater. Res. Bull.* **11**(5), 559–566 (1976). [https://doi.org/10.1016/0025-5408\(76\)90239-7](https://doi.org/10.1016/0025-5408(76)90239-7)



25. G. Newman, L. Klemann, Ambient-temperature cycling of an Na-TiS₂ cell. *J. Electrochem. Soc.* **127**(10), 2097–2099 (1980). <https://doi.org/10.1149/1.2129353>
26. L. Conroy, K. Park, Electrical properties of group IV disulfides TiS₂, ZrS₂, HfS₂, and SnS₂. *Inorg. Chem.* **7**(3), 459–463 (1968). <https://doi.org/10.1021/ic50061a015>
27. M. Dresselhaus, I. Thomas, Alternative energy technologies. *Nature* **414**, 332–337 (2001). <https://doi.org/10.1038/35104599>
28. J. Trevey, C. Stoldt, S. Lee, High power nanocomposite TiS₂ cathodes for all-solid-state lithium batteries. *J. Electrochem. Soc.* **158**(12), A1282–A1289 (2011). <https://doi.org/10.1149/2.017112jes>
29. A. Let, D. Mainwaring, C. Rix, P. Murugaraj, Thio sol-gel synthesis of titanium disulfide thin films and powders using titanium alkoxide precursors. *J. Non-Cryst. Solids* **354**(15), 1801–1807 (2008). <https://doi.org/10.1016/j.jnoncrysol.2007.09.005>
30. A. Huckaba, S. Gharibzadeh, M. Ralaiarisoa, C. Roldán-Carmona, N. Mohammadian et al., Low-cost TiS₂ as hole-transport material for perovskite solar cells. *Small Methods* **1**(10), 1700250 (2017). <https://doi.org/10.1002/smt.20170250>
31. A. Huckaba, M. Ralaiarisoa, K. Cho, E. Oveisi, N. Koch, M. Nazeeruddin, Intercalation makes the difference with TiS₂: boosting electrocatalytic water oxidation activity through co intercalation. *J. Mater. Res.* **33**(5), 528–537 (2017). <https://doi.org/10.1557/jmr.2017.431>
32. J. Ni, S. Fu, C. Wu, J. Maier, Y. Yu, L. Li, Self-supported nanotube arrays of sulfur-doped TiO₂ enabling ultrastable and robust sodium storage. *Adv. Mater.* **28**(11), 2259–2265 (2016). <https://doi.org/10.1002/adma.201504412>
33. C. McManamon, J. O'Connell, P. Delaney, S. Rasappa, J.D. Holmes, M.A. Morris, A facile route to synthesis of S-doped TiO₂ nanoparticles for photocatalytic activity. *J. Mol. Catal. A: Chem.* **406**, 51–57 (2015). <https://doi.org/10.1016/j.molcata.2015.05.002>
34. L.G. Devi, R. Kavitha, Enhanced photocatalytic activity of sulfur doped TiO₂ for the decomposition of phenol: a new insight into the bulk and surface modification. *Mater. Chem. Phys.* **143**(3), 1300–1308 (2014). <https://doi.org/10.1016/j.matchemphys.2013.11.038>
35. S. Laruelle, S. Grugeon, P. Poizot, M. Dolle, L. Dupont, J.M. Tarascon, On the origin of the extra electrochemical capacity displayed by mo/li cells at low potential. *J. Electrochem. Soc.* **149**(5), A627–A634 (2002). <https://doi.org/10.1149/1.1467947>
36. Y. Liu, H. Wang, L. Cheng, N. Han, F. Zhao et al., TiS₂ nanoplates: a high-rate and stable electrode material for sodium ion batteries. *Nano Energy* **20**, 168–175 (2016). <https://doi.org/10.1016/j.nanoen.2015.12.028>
37. L. Wu, D. Bresser, D. Buchholz, A.G. Guinevere, R.C. Claudia, A. Ochel, S. Passerini, Unfolding the mechanism of sodium insertion in anatase TiO₂ nanoparticles. *Adv. Energy Mater.* **5**(2), 1401142 (2014). <https://doi.org/10.1002/aenm.201401142>
38. K. Lan, Y. Liu, W. Zhang, Y. Liu, A. Elzatahry et al., Uniform ordered two-dimensional mesoporous TiO₂ nanosheets from hydrothermal-induced solvent-confined monomicelle assembly. *J. Am. Chem. Soc.* **140**(11), 4135–4143 (2018). <https://doi.org/10.1021/jacs.8b00909>
39. M. Tahir, B. Oschmann, D. Buchholz, X. Dou, I. Lieberwirth et al., Extraordinary performance of carbon-coated anatase TiO₂ as sodium-ion anode. *Adv. Energy Mater.* **6**(4), 1501489 (2015). <https://doi.org/10.1002/aenm.201501489>
40. H. Lindström, S. Södergren, A. Solbrand, H. Rensmo, J. Hjelm, A. Hagfeldt, S.-E. Lindquist, Li⁺ ion insertion in TiO₂ (anatase). 2. Voltammetry on nanoporous films. *J. Phys. Chem. B* **101**(39), 7717–7722 (1997). <https://doi.org/10.1021/jp970490q>
41. V. Augustyn, J. Come, M.A. Lowe, J.W. Kim, P.-L. Taberna et al., High-rate electrochemical energy storage through Li⁺ intercalation pseudocapacitance. *Nat. Mater.* **12**, 518–522 (2013). <https://doi.org/10.1038/nmat3601>
42. K. Brezesinski, J. Wang, J. Haetge, C. Reitz, S.O. Steinmüller et al., Pseudocapacitive contributions to charge storage in highly ordered mesoporous group V transition metal oxides with iso-oriented layered nanocrystalline domains. *J. Am. Chem. Soc.* **132**(20), 6982–6990 (2010). <https://doi.org/10.1021/ja9106385>
43. C. Zhao, C. Yu, M. Zhang, H. Huang, S. Li et al., Ultrafine MoO₂-carbon microstructures enable ultralong-life power-type sodium ion storage by enhanced pseudocapacitance. *Adv. Energy Mater.* **7**(15), 1602880 (2017). <https://doi.org/10.1002/aenm.201602880>
44. L. Que, F. Yu, Z. Wang, D. Gu, Pseudocapacitance of TiO_{2-x}/CNT anodes for high-performance quasi-solid-state li-ion and na-ion capacitors. *Small* **14**(17), 1704508 (2018). <https://doi.org/10.1002/sml.201704508>
45. T. Brezesinski, J. Wang, J. Polleux, B. Dunn, S.H. Tolbert, Templated nanocrystal-based porous TiO₂ films for next-generation electrochemical capacitors. *J. Am. Chem. Soc.* **131**(5), 1802–1809 (2009). <https://doi.org/10.1021/ja8057309>
46. Y. Xiong, J. Ian, Y. Cao, X. Ai, H. Yang, Electrospun TiO₂/C nanofibers as a high-capacity and cycle-stable anode for sodium-ion batteries. *ACS Appl. Mater. Interfaces* **8**(26), 16684–16689 (2016). <https://doi.org/10.1021/acsami.6b03757>
47. Y. Wu, X. Liu, Z. Yang, L. Gu, Y. Yu, Nitrogen-doped ordered mesoporous anatase TiO₂ nanofibers as anode materials for high performance sodium-ion batteries. *Small* **12**(26), 3522–3529 (2016). <https://doi.org/10.1002/sml.201600606>
48. Q. Zhao, R. Bi, J. Cui, X. Yang, L. Zhang, TiO_{2-x} nanocages anchored in N-doped carbon fiber films as a flexible anode for high-energy sodium-ion batteries. *ACS Appl. Energy Mater.* **1**(9), 4459–4466 (2018). <https://doi.org/10.1021/acsaem.8b00985>
49. N. Lee, J. Jung, J. Lee, H. Jang, I.D. Kim, W.H. Ryu, Facile and fast na-ion intercalation employing amorphous black TiO_{2-x}/C composite nanofiber anodes. *Electrochim. Acta* **263**, 417–425 (2018). <https://doi.org/10.1016/j.electacta.2018.01.085>